

Widely Extended [OIII] 88 μm Line Emission around the 30 Doradus Region Revealed with AKARI FIS-FTS

Mitsunobu KAWADA *, Ai TAKAHASHI, Akiko YASUDA, Yuichi KIRIYAMA, Tatsuya MORI,
Akio MOURI, Hidehiro KANEDA

Graduate School of Science, Nagoya University, Furo-cho, Chikusa-ku, Nagoya 464-8602, Japan

Yoko OKADA

I. Physikalisches Institut, Universität zu Köln, Zùlpicher Str. 77, 50937 Köln, Germany

Hidenori TAKAHASHI

*Gunma Astronomical Observatory, 6860-86 Nakayama, Takayama, Agatsuma, Gunma 377-0702,
Japan*

and

Noriko MURAKAMI

Bisei Astronomical Observatory, 1723-70 Okura, Bisei-cho, Ibara-shi, Okayama 714-1411, Japan

(Received ; accepted)

Abstract

We present the distribution map of the far-infrared [OIII] 88 μm line emission around the 30 Doradus (30 Dor) region in the Large Magellanic Cloud obtained with the Fourier Transform Spectrometer of the Far-Infrared Surveyor onboard AKARI. The map reveals that the [OIII] emission is widely distributed by more than 10' around the super star cluster R136, implying that the 30 Dor region is affluent with interstellar radiation field hard enough to ionize O²⁺. The observed [OIII] line intensities are as high as $(1 - 2) \times 10^{-6} \text{ W m}^{-2} \text{ sr}^{-1}$ on the peripheral regions 4' - 5' away from the center of 30 Dor, which requires gas densities of 60 - 100 cm⁻³. However the observed size of the distribution of the [OIII] emission is too large to be explained by massive stars in the 30 Dor region enshrouded by clouds with the constant gas density of 10² cm⁻³. Therefore the surrounding structure is likely to be highly clumpy. We also find a global correlation between the [OIII] and the far-infrared continuum emission, suggesting that the gas and dust are well mixed in the highly-ionized region where the dust survives in clumpy dense clouds shielded from the energetic photons.

Key words: ISM: HII regions — ISM: lines and bands — galaxies: Magellanic Clouds

* Present Address: Institute of Space Astronautical Science (ISAS) / JAXA, 3-1-1 Yoshinodai, Chuo-ku, Sagami-hara 252-5210, Japan; e-mail: kawada@ir.isas.jaxa.jp

1. Introduction

Star forming regions and interstellar media have been well studied in all the wavelength regimes from radio to γ -ray. An advantage using far-infrared (far-IR) light is that we can trace photo-ionization and dissociation regions without needing to correct for extinction. In the far-IR region, there are important forbidden lines of atoms and ions, such as [OI] $63\mu\text{m}$, $146\mu\text{m}$, [OIII] $88\mu\text{m}$, [NII] $122\mu\text{m}$, $205\mu\text{m}$, and [CII] $158\mu\text{m}$, which are good tracers of the interstellar media in various gas phases.

30 Doradus (30 Dor) in the Large Magellanic Cloud (LMC) is one of the most famous massive star forming regions (e.g. Kennicutt 1984). Its distance is about 50 kpc and the physical scale of $1'$ corresponds to 15 pc. In the center, as revealed by the Hubble Space Telescope, there are a lot of massive stars in a compact region, which is named the R136 super star cluster (Selman et al. 1999; Massey & Hunter 1998). The bubble of $1'$ in diameter exists around the center of R136, where gas is almost completely evacuated (Indebetouw et al. 2009; Rubio et al. 1998). Prominent X-ray and $\text{H}\alpha$ filamentary and/or shell structures are extended in the north and the west direction from the center (Townsend et al. 2006). In the optical emission lines such as [SII] $\lambda 6724\text{\AA}$ and [OIII] $\lambda 5007\text{\AA}$, widely extended components of ionized gas were revealed around the 30 Dor region by the University of Michigan/CTIO Magellanic Cloud Emission Line Survey (MCELS; Smith et al. 2000).

From the early era of IR astronomy, the 30 Dor region has been studied by various IR observations. Using the FIFI instrument of the Kuiper Airborne Observatory (KAO), Poglitsch et al. (1995) observed the far-IR forbidden lines of [CII] $158\mu\text{m}$ and [OI] $63, 146\mu\text{m}$ in the 30 Dor region, and made a line intensity map of [CII] $158\mu\text{m}$ with an arc-minute spatial resolution over $7' \times 7'$ area. Balloon-borne IR telescopes, such as Balloon-borne Infrared Carbon Explore (BICE), observed the LMC region. BICE mapped the entire area of the LMC by the [CII] line with a beam of about $15'$ size. Rubin et al. (2009) discussed the photoelectric heating and [CII] cooling in the LMC. The first powerful tool for IR spectroscopy was provided by the Infrared Space Observatory (ISO) operated in the late 1990s. The ISOCAM made line intensity maps of [NeII] $12.81\mu\text{m}$ and [NeIII] $15.56\mu\text{m}$ emission lines for the central $\sim 3'$ area of the 30 Dor region (Madden et al. 2006). The ionization potentials of Ne and Ne^+ are 21.56 and 40.96 eV, respectively. Therefore, the [NeII] and [NeIII] lines are good tracers of highly-ionized gas, similarly to the [OIII] line with the ionization potential of 35.12 eV. In the far-IR, the ISO/LWS observed more than 10 points with different physical conditions for the 30 Dor region (Vermeij et al. 2002; Vermeij & van der Hulst 2002). However, the spatial information provided by the ISO/LWS was rather poor, because these observations were performed by a single beam.

For technical reasons, far-IR spectral mapping observations with high spatial resolution were difficult. After ISO, AKARI takes a unique position in the far-IR spectroscopy. The Japanese IR astronomical satellite, AKARI (Murakami et al. 2007), which was launched on

February 21, 2006 (UT), has two kinds of focal-plane instruments; Infrared Camera (IRC) (Onaka et al. 2007) and Far-Infrared Surveyor (FIS) (Kawada et al. 2007), to cover the whole IR regime from 2 to 180 μm . Far-IR spectroscopic capability of AKARI is realized by a Fourier transform spectrometer (FTS) as a function of the FIS (Kawada et al. 2008). The advantage of FIS-FTS over the ISO/LWS is an imaging spectroscopic capability with higher spatial resolution; each pixel of the FIS-FTS detector arrays can simultaneously take a spectrum with about $40''$ (FWHM) angular resolution, while the ISO/LWS has the single beam of $80''$ in FWHM. The physical scales corresponding to their resolutions in the LMC are about 10 pc and 20 pc for FIS-FTS and the ISO/LWS, respectively.

Spectral maps with high spatial resolution are essential to investigate the interstellar media, especially those around ionized regions. The structure of an ionized region is determined by the locations of ionizing stars and the distribution of the ambient interstellar media. High spatial resolution maps of the far-IR lines clearly show the structure of star forming regions relating to the environment of star formation. Spitzer Space Telescope made spectral line maps of 30 Dor by using the IRS and the MIPS in a SED mode in the Spitzer legacy survey of the LMC: Surveying the Agents of a Galaxy's Evolution (SAGE; Meixner et al. 2006), which revealed the ionization state of the 30 Dor region and super star cluster R136 (Indebetouw et al. 2009). AKARI FIS-FTS observed many local regions distributed around the 30 Dor region and provided their spectral maps. In this paper, we present the large-scale spatial distribution of the [OIII] $88\mu\text{m}$ line emission around the 30 Dor region.

The advantage of the AKARI [OIII] data over the ISOCAM [NeIII] and the Spitzer data is the spatial coverage of much wider areas, i.e., those far outside the bubbles around 30 Dor. Thus our data provide information on the ISM influenced by intense radiation from massive stars rather than shocks by stellar winds and supernovae in R136. The optical [OIII] map with MCELS also covers a large area. As compared to the far-IR [OIII] map, the optical map has a higher spatial resolution, but suffers extinction effects in dense gas regions, which may hamper accurate measurements of the change of the line intensity with the distance from R136.

2. Observations

AKARI carried out far-IR spectroscopic observations from April 2006 to August 2007. As a result, about 600 pointed observations were performed with FIS-FTS. More than two thirds of the FIS-FTS observations were parallel observations with the IRC, in which the IRC has priority for observations. Since the fields-of-view (FOVs) of the IRC and the FIS are separated by about half a degree, FIS-FTS observed off-primary target skies in the parallel observations. Yet these data are useful as a spectroscopic survey of the diffuse interstellar medium, since many IRC observations concentrate on the Galactic plane and the LMC.

In this paper, we selected 14 pointed observations around the 30 Dor regions, which targeted relatively bright regions among the FIS-FTS observations of the LMC. An observa-

Table 1. Observation log

No.	date	position (J2000.0)*	obs. param. [†]	comment [‡]	det. limit [§]
1	2006/10/14-21:15	(84.74402, -69.67834)	SED, 0.5s	IRC04 (b;Ns)	3.9
2	2006/10/19-21:57	(85.20209, -69.57140)	SED, 0.5s	IRC04 (b;Ns)	1.1
3	2006/10/21-21:54	(85.13556, -69.52066)	SED, 0.5s	IRC02 (b;N)	1.7
4	2006/10/23-18:32	(84.85551, -69.45006)	SED, 0.5s	IRC02 (b;N)	1.1
5	2006/10/23-20:11	(85.16322, -69.07068)	SED, 0.5s	IRC04 (b;Ns)	3.4
6	2006/10/24-21:00	(85.09940, -69.17079)	SED, 0.5s	IRC02 (b;N)	1.1
7	2006/10/25-18:29	(84.58520, -69.37970)	SED, 0.5s	IRC02 (b;N)	1.2
8	2006/10/25-21:48	(84.70576, -69.23942)	SED, 0.5s	IRC02 (b;N)	1.0
9	2006/10/26-20:57	(84.30852, -69.30413)	SED, 0.5s	IRC02 (b;N)	0.9
10	2006/10/26-22:36	(84.95287, -68.95736)	SED, 0.5s	IRC02 (b;N)	1.1
11	2006/10/27-20:06	(84.56963, -69.02005)	SED, 0.5s	IRC02 (b;N)	1.4
12	2006/10/27-21:45	(84.03696, -69.22217)	SED, 0.5s	IRC02 (b;N)	1.2
13	2006/10/29-20:03	(84.20209, -69.08269)	SED, 0.5s	IRC02 (b;N)	1.0
14	2006/10/30-20:51	(83.81157, -69.14057)	SED, 0.5s	IRC02 (b;N)	1.3

* Equatorial coordinates of the center of the short-wavelength-band array

[†] Operational parameters of FIS-FTS; spectral resolution mode and reset interval (see Kawada et al. 2007)

[‡] Astronomical observation template of the IRC (Onaka et al. 2007) in a parallel observation

[§] Typical 3σ detection limit of the [OIII] $88\mu\text{m}$ line [$\times 10^{-7} \text{ W m}^{-2} \text{ sr}^{-1}$]

tion log is summarized in table 1, and observed areas are shown in figure 1, plotted on the Spitzer/MIPS $24\mu\text{m}$ map from the SAGE program. For comparison, the observational positions of the ISO/LWS are marked by the small open circles with a size of the beam, and the area of the spectral mapping with the Spitzer/MIPS in a SED mode is indicated by the rectangle in the center of 30 Dor.

Although our observations do not cover the center of 30 Dor, they cover wide areas around the 30 Dor region and the south ridge. As shown in figure 1, our observational areas are located on the periphery of the area covered with Spitzer and thus complementary to the Spitzer observations. Each observing point has 60 pixels with a FOV of $30'' \times 30''$ for each pixel in the short wavelength band, and 45 pixels with a $50'' \times 50''$ pixel FOV in the long wavelength band. All the observational data analyzed in this paper are taken in a low resolution mode (named SED mode), whose spectral resolution is about 1.2 cm^{-1} .

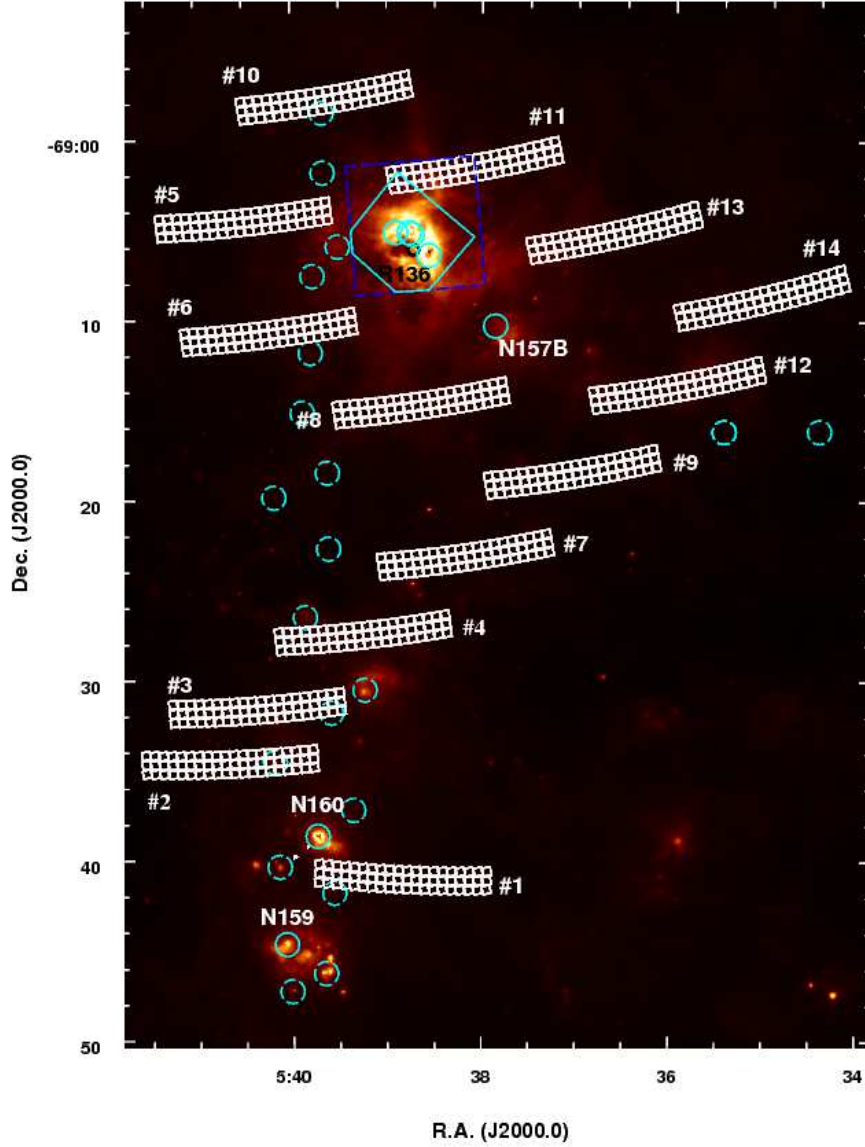


Fig. 1. Observational areas with FIS-FTS overlaid on the Spitzer MIPS $24\mu\text{m}$ map from the SAGE archives. Each observing point is indicated by the white frame in the 20×3 array format of the short-wavelength-band detector labeled with the number listed in table 1. The observational points of the ISO/LWS are also plotted by the open circles with a size of the beam; the line intensities from the solid circles are reported by Vermeij et al. (2002), while those from the dashed circles are not reported in any papers listed in the ISO archives database. The dashed square and the solid rectangle at the center of 30 Dor indicate the coverage of spectral mapping with the Spitzer/IRC and the MIPS in a SED mode, respectively (Indebetouw et al. 2009).

3. Data Reduction

We used the standard reduction tools for FIS-FTS to derive spectra. Details of the standard tools are described in the AKARI FTS Toolkit Manual¹. Here, we briefly explain the way to obtain spectra from raw signal and to extract emission lines from the spectra.

Raw data are processed through the standard pipeline tools, in which a linearity correction, glitch removing and a correction of the optical path difference (OPD) are performed with an eye-ball check. Then, a set of interferograms for each pixel is derived. Interferograms are transformed to raw spectra by applying a discrete Fourier transformation at the second stage of the pipeline, where the adopting OPD range and the apodizing function are selectable. In this paper, we applied a box-type apodizing function and used data in an OPD range of ± 0.35 cm for the short wavelength band, a little shorter than the full range (± 0.42 cm), to avoid a channel fringe (Kawada et al. 2008). The resulting spectral resolution of the short wavelength band is reduced to ~ 1.4 cm⁻¹ from ~ 1.2 cm⁻¹ of the full performance for the flat apodization. In the final step of the pipeline, raw spectra are converted to sky spectra by correcting for instrumental factors. Details of the calibration scheme of FIS-FTS and the accuracy are described in Murakami et al. (2010).

Since 30 forward and backward scans are obtained by a single pointed observation, there is a set of 60 spectra for each pixel. From the set of the spectra, we calculated an average spectrum and estimated the error of each spectral element. Figure 2 shows examples of the averaged spectra obtained in the short wavelength band, exhibiting the clear detection of the [OIII] 88 μ m line at 113 cm⁻¹ wavenumber. The structure around the line indicates a sinc function due to the box-type apodizing function. Dust continuum emissions are also detected; the SW26 and SW45 pixels show relatively flat spectra, while the continuum spectrum of the SW28 pixel indicates a cooler dust temperature. From these spectra, we extracted [OIII] line intensities by simply subtracting continuum emissions from the signals integrated over 111.0 – 114.5 cm⁻¹. The contribution of the continuum emissions at the line position is estimated from signals in both sides of the line, 90.0 – 111.0 cm⁻¹ and 114.5 – 130.0 cm⁻¹. The detection limit depends on the sensitivity of each pixel and also on the environmental condition of observations. The 3σ detection limits of the [OIII] line listed in table 1 are median values of array pixels for each pointed observation estimated from errors at the [OIII] line. The minimal 3σ detection limit is about 0.6×10^{-7} W m⁻² sr⁻¹, and a typical value is about 1×10^{-7} W m⁻² sr⁻¹.

We also obtain spectra in the long wavelength band, which include the [CII] 158 μ m line emission detected in many observations. However, due to the non-uniformity of the detector performance among the pixels, the spectral data are still not well calibrated to discuss the spatial distribution of the [CII] line. Therefore, in this paper, we treat only the [OIII] 88 μ m line, which traces highly-ionized gas. The [OIII] 88 μ m intensity map thus obtained is shown

¹ AKARI (ASTRO-F) Observers Page – <http://www.ir.isas.jaxa.jp/ASTRO-F/Observation/>

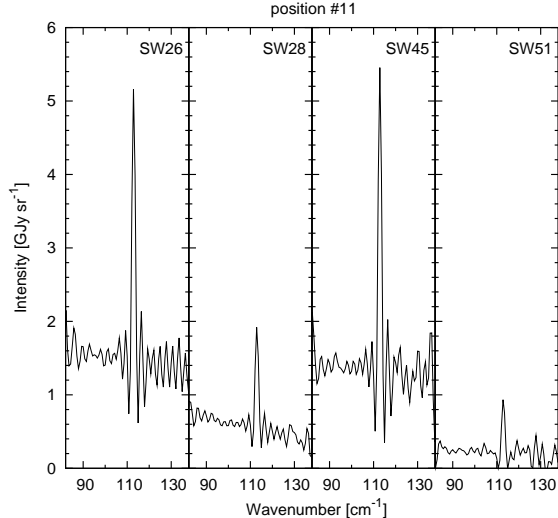


Fig. 2. Examples of the spectra of 4 pixels in the short wavelength band obtained from the observation #11. The [OIII] line at 113 cm^{-1} ($88 \mu\text{m}$) and continuum emissions with different slopes are clearly detected.

in figure 3 together with the MIPS $24\mu\text{m}$ intensity contour map. The [OIII] map is created by re-gridding pixel data on the astronomical coordinates and masking those with signal-to-noise ratios less than two. The MIPS $24\mu\text{m}$ contour map in the figure is convolved with a Gaussian kernel whose width match the spatial resolution of the FIS ($\sim 40''$). The map clearly shows widely distributed [OIII] $88\mu\text{m}$ line emission with arc-minute scale structures around 30 Dor. From ISO archival data, we find that the ISO/LWS barely detects the [OIII] $88\mu\text{m}$ line emission at the position in the FIS-FTS # 3 area (see figure 1) with the intensity of about $2 \times 10^{-8} \text{ W m}^{-2} \text{ sr}^{-1}$, which is below our typical 3σ detection limits as shown in table 1. The map in figure 3 is consistent with the ISO measurement. This line intensity level represents that from quiescent parts of the LMC and the intensities of the spatially extended emission seen in figure 3 are 5 – 200 times higher than this level.

4. Results

4.1. [OIII] Intensity Map

We significantly detect the [OIII] $88\mu\text{m}$ emission at many pixels in each pointed observation. Figure 3 shows the global structure of the [OIII] emission in about one square degree; the emission region of the [OIII] line is extended around the 30 Dor region more widely than the area covered with the Spitzer/MIPS in a SED mode. The structure of the [OIII] line emission, the highly-ionized region, is well correlated with that of MIPS $24\mu\text{m}$ (contours) tracing hot dust emission around the 30 Dor region. In particular, a filamentary structure at the northern part seen in the MIPS $24\mu\text{m}$ contours is also recognized well in the [OIII] intensity map (obs.#10

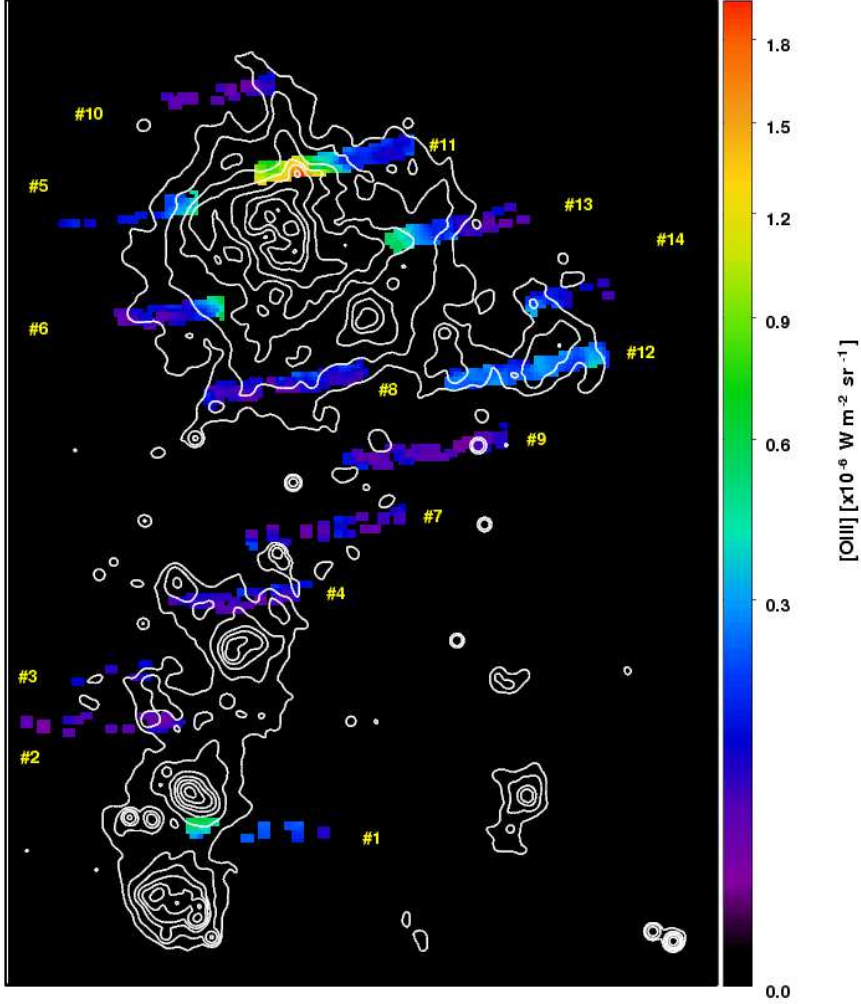


Fig. 3. [OIII] 88 μ m line intensity map, shown together with the MIPS 24 μ m contour map whose spatial resolution is reduced to the same as the [OIII] map.

& #11). Spitzer obtained spectra in the 30 Dor region with the IRS and the MIPS in a SED mode. The [OIII] 88 μ m intensity map taken by the MIPS covers the center of 30 Dor (rectangle in figure 1), partially overlapped with our map at the north edge. The MIPS measurement shows values about three times larger than ours, but both are roughly consistent by considering large uncertainties of our absolute line intensity calibration (Murakami et al. 2010). Owing to our clear detection outside the Spitzer observing area, we reveal the widely extended structure of the highly-ionized region. In particular, the ionized regions are extended in the north and the west direction along the MIPS 24 μ m structures, which have spatial correspondence to the X-ray and H α filamentary structures.

On the other hand, the south-west region (obs.#12 & #14) outside the 30 Dor does not have a clear correlation between the [OIII] 88 μ m and the MIPS 24 μ m emissions. We also detect the [OIII] emission significantly from this region, whose distribution is rather flat as compared

to the MIPS $24\mu\text{m}$. This region contains the 30 Dor C superbubble, which is a large (45 pc radius) shell of material swept up by fast stellar winds and supernovae from tens of massive stars in an OB association. There is a mixture of thermal and nonthermal X-ray emission (Bamba et al. 2004; Townsley et al. 2006, Yamaguchi et al. 2009); any photoionization in this region may receive a contribution by hard radiation from the supernova remnants. There is probably also direct collisional ionization to O^{2+} . The south region far outside 30 Dor (obs.#1 – #4, #7 & #9) may have a different relation from the region near 30 Dor. At least, the obs.#1 data are apparently influenced by N159 and N160, other massive star forming regions (see figure 1). The MIPS $24\mu\text{m}$ emission regions in the south are compact as compared to the 30 Dor region. There are extended molecular clouds in this region and ionizing stars are located in dense cores, suggesting that star formation is in an early stage.

For clarity of presentation, we categorize the observational points into four groups according to their positions with respect to 30 Dor. The NW group (obs.#10, #11 and #13) is located in the north-west region of 30 Dor and has a good correlation with the MIPS $24\mu\text{m}$ surface brightness. The SW group (obs.#12 and #14) is located on the far west side of 30 Dor and has a rather flat distribution of the [OIII] line emission. The SE group (obs.#5, #6 and #8) is located in the south-east region of 30 Dor. The SR group (obs.#1 – #4, #7 and #9) is located along the south ridge of molecular clouds.

4.2. Point to Point Correlations

Figure 4 shows a scatter plot between the [OIII] $88\mu\text{m}$ line intensity and the $\text{H}\alpha$ intensity, where the $\text{H}\alpha$ data are taken from the Southern H-Alpha Sky Survey Atlas (Gaustad et al. 2001). The different colors correspond to the data from the different group defined above. We can see a global correlation between the [OIII] and $\text{H}\alpha$ emissions for a range of about one and a half orders of magnitude. The correlation, however, is not so tight at the higher line intensity region. A possible reason is difference in ionization degrees of the gases associated with the $\text{H}\alpha$ and [OIII] $88\mu\text{m}$ emission; much higher energies of photons (> 35.12 eV) are required to ionize O^+ to O^{2+} than to ionize H atom.

We also make a scatter plot between the continuum emission at $88\mu\text{m}$ derived with FIS-FTS and the MIPS $24\mu\text{m}$ emission, as shown in figure 5. The spatial resolution of the MIPS $24\mu\text{m}$ map is reduced to match the FIS-FTS map. There is a tight correlation between the two continuum emissions at $24\mu\text{m}$ and $88\mu\text{m}$ for about two orders of magnitude. Thus the $88\mu\text{m}$ continuum signal detected with FIS-FTS reasonably traces dust emission. As shown in the plot, brighter regions exhibit a little bluer colors, indicating hotter dust temperatures, and thus stronger radiation field. All the data points in every group are on almost the same relation, suggesting that the properties of dust are similar throughout the 30 Dor region.

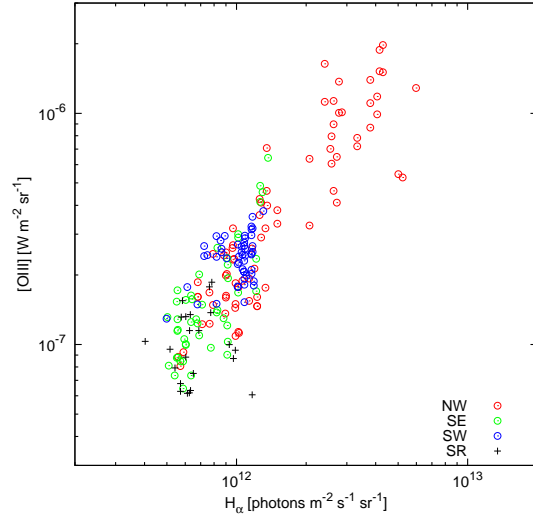


Fig. 4. Scatter plot between the [OIII] line emission and the H α emission. The different marks and colors correspond to the data from the different regions of the observed area (see text).

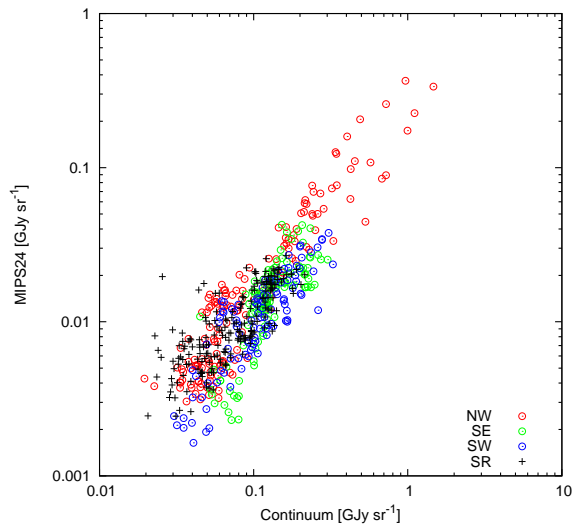


Fig. 5. Scatter plot between the continuum emission at 88 μ m detected with FIS-FTS and the MIPS 24 μ m emission. The spatial resolution of the MIPS 24 μ m map is reduced to matched the FIS-FTS map. The colors of the data points are the same as in figure 4.

5. Discussion

We reveal the extended distribution of the [OIII] emission around the 30 Dor region; the distribution is found to be much wider than the boundary of the previously observed area. Even on the peripheral regions $4' - 5'$ away from the center of 30 Dor, we obtain [OIII] line intensities so high as $(1 - 2) \times 10^{-6} \text{ W m}^{-2} \text{ sr}^{-1}$. From calculation of a three-level system for the lowest energy levels of O^{2+} (Mendoza 1983), we estimate that the gas densities of $60 - 100 \text{ cm}^{-3}$ are required to explain the above line intensities. Here we assume that 50 % of oxygen is in the ionization state of O^{2+} and the O/H abundance ratio is 2.3×10^{-4} (Madden et al. 2006). For the depth of the emitting region, we adopt 75 pc ($=5'$), which is similar to the distance from the center of 30 Dor.

To ionize O^+ to O^{2+} , energetic photons ($> 35.12 \text{ eV}$) are required, which can be produced only by very massive stars such as early O type stars and Wolf-Rayet (WR) stars. We estimate the contribution of the massive stars to the ionization of O^+ . R136 has a lot of massive stars in the compact central region, as revealed by the Hubble Space Telescope (Selman et al. 1999; Massey & Hunter 1998). The ionization structure at 30 Dor (a few arc-minutes around R136) is determined by a balance between radiation from massive stars in R136 and the distribution of the interstellar medium (Poglitsch et al. 1995; Indebetouw et al. 2009).

To assess the influence range of radiation field from the R136 super star cluster, we investigate the change of the [OIII] intensity with distance from R136. Figure 6 shows the radial profiles of the distributions of the [OIII] emission and the far-IR continuum emission plotted against the distance from R136. The upper plots (filled circles) show the [OIII] line emission profile, while the lower plots (open circles) show the far-IR continuum emission profile. The SR group is excluded in this plot. The [OIII] emission and far-IR continuum of the NW and SE groups show a clear dependence on the distance from R136 as seen in figure 6, while those of the SW group do not; the latter is likely to have local ionization sources other than R136.

Figure 6 shows the wide distribution of the highly-ionized region around the central super star cluster R136. The influence of R136 seems to reach $\sim 10'$, or 150 pc away from R136. The intensities of the central [OIII] emission detected with the ISO/LWS are consistent with the extrapolation of the AKARI/FIS-FTS data to the inner area of $1'$ from R136, as shown in figure 6. The ISO/LWS data point labeled N157B is located on the supernova remnant NGC2060 (see figure 1). It is notable that the far-IR continuum emission has a radial dependence similar to the [OIII] emission. The vertical line in the figure indicates the Strömngren radius of hydrogen gas (about $2'$) determined by the R136 super star cluster. To calculate the value, we assume that the massive stars within a radius of 15 pc ($1'$) (Bonanos et al. 2009; Selman et al. 1999; Massey & Hunter 1998) concentrate on the center and that ambient gas density and temperature are 100 cm^{-3} and 10^4 K , respectively. The gas density adopted here reflects the above value that

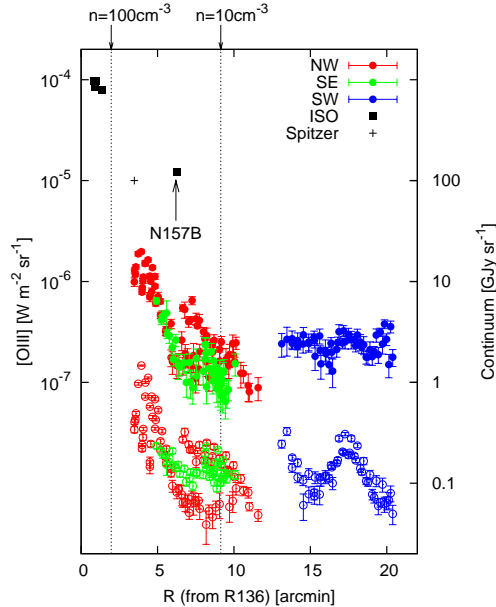


Fig. 6. Radial profiles of the distributions of the [OIII] line emission (filled circles) and far-IR continuum (open circles) plotted against the distance from the super star cluster R136. ISO/LWS observations of 30 Dor are plotted with the filled squares as a reference of the central region (Vermeij et al. 2002). Note that the ISO/LWS data point labeled N157B is located on the supernova remnant NGC2060 (see figure 1). The plus (+) indicates the result of the Spitzer/MIPS observation in the SED mode (Indebetouw et al. 2009). Strömgren radii of R136 for ambient gas densities of 100 cm^{-3} and 10 cm^{-3} are plotted by the dotted lines.

is estimated from the [OIII] line intensity observed with FIS-FTS. These gas parameters are also reasonable from the results obtained with the radio (Peck et al. 1997), ISO (Vermeij & van der Hulst 2002), and Spitzer observations (Indebetouw et al. 2009), which suggested densities around 200 cm^{-3} near the center of 30 Dor. We consider a conservative case that the gas density is constant at the value estimated in the peripheral region. Yet, from figure 6, it is clear that the simple calculation cannot explain the widely-extended distribution of the [OIII] line emission. The central bubble of $1'$ in diameter would increase the Strömgren radius, but its presence does not dramatically change the result. To explain the observed distribution, we have to assume a lot of hidden massive stars, and/or non-uniform distribution of the interstellar media, that is, clumpy distribution and leakage of ionizing photons. It is not likely that a lot of embedded massive stars are hidden in the field. If the gas density is reduced down to 10 cm^{-3} , the Strömgren radius expands to $9'$, which is comparable to the observed size of the distribution of the [OIII] emission. Therefore a picture of the clumpy distribution of the interstellar media with a volume filling factor of ~ 0.1 is a plausible explanation.

Thus it is difficult to explain the ionization in the areas far away from 30 Dor solely by radiation from massive stars in R136. However many other massive stars are also distributed

widely in the 30 Dor region in addition to those in R136. Bonanos et al. (2009) presented a catalog of 1750 massive stars in the LMC with accurate spectral types; stars in the R136 super star cluster are not included in the catalog. We calculated the Strömgren radius of hydrogen gas for each cataloged star (Vacca et al. 1996), assuming the physical condition of 100 cm^{-3} and 10^4 K for gas density and temperature, respectively. The gas density again corresponds to the value obtained from the observed [OIII] line intensity. The Strömgren radius thus obtained is plotted in figure 7 with the circle for each massive star. So far the Strömgren radii are calculated for H^+ ions, but not for O^{2+} ions. However our simplified calculation shows that the Strömgren radius for O^{2+} is almost the same as for H^+ as long as ionizing photons have energies significantly higher than the O^+ ionization energy (35.12 eV). At least, a Strömgren radius for O^{2+} is no larger than that for H^+ ions. Thus it is difficult to explain the observed [OIII] emission in the outer region of 30 Dor by radiation from the distributed massive stars, too.

In order to evaluate the contribution of hidden sources of ionization to the observed distribution of the [OIII] line emission, in figure 8, we plot the [OIII] line intensity as a function of the O^+ -ionizing photon flux expected from the cataloged stars. We obtain the flux at each position by adding the total absorption-free photon fluxes coming from the cataloged WR stars and O2–O7 stars shown in figure 7. Here we use the projected distance for each star. As seen in the figure, there is a correlation between the [OIII] line intensity and the absorption-free ionizing flux, at least for the NW region and part of the SE region. This suggests that the ISM is very clumpy in those regions and that there are no significant hidden sources of ionization other than the dense star clusters in figure 7. An exception is the SW region that contains 30 Dor C, where the [OIII] line emission shows almost no dependence on the ionizing photon flux with line intensities above and below the correlation at smaller and larger photon fluxes, respectively. The lack of the correlation suggests the presence of another diffuse ionizing source, which can be attributed to hard radiation and/or shocks from the supernova remnants 30 Dor C. As for the lower line intensities at photon larger fluxes, some areas of the SW region are so closely located near massive stars (see figure 7) that the photon fluxes calculated from the projected distances are very likely overestimated.

Figure 9 shows a scatter plot between the [OIII] line and the $88 \mu\text{m}$ continuum emission, both obtained with FIS-FTS, where we see an overall correlation between them. It is consistent with the similar trend of radial dependence between the [OIII] emission and the continuum emission as seen in figure 6. This correlation is interesting because they are likely of different origins; the far-IR continuum represents the dust emission mostly coming from neutral regions, while the [OIII] emission originates in highly-ionized gas regions. Thus the correlation suggests that the highly-ionized gas and dust are mixed well and exist in the same region, or have a clumpy structure where the dust is shielded from energetic photons by local dense gases. This interpretation is consistent with the widely extended distribution of the [OIII] emission.

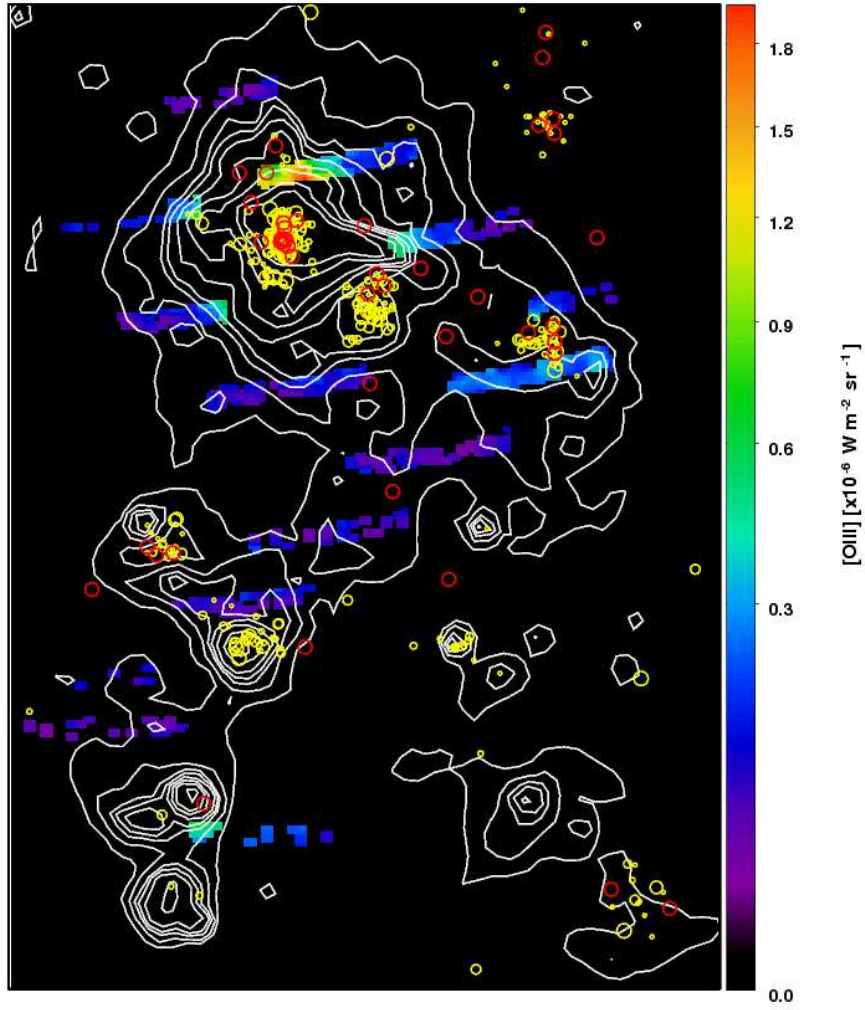


Fig. 7. Sizes of the Strömberg spheres for cataloged Wolf-Rayet stars (red or dark circles) and O2–O7 stars (yellow or bright circles) calculated under the assumption of $n = 100 \text{ cm}^{-3}$ and $T = 10^4 \text{ K}$ for ambient gas. The [OIII] intensity map is the same as in figure 3, but the contours show the $H\alpha$ emission (Gaustad et al. 2001).

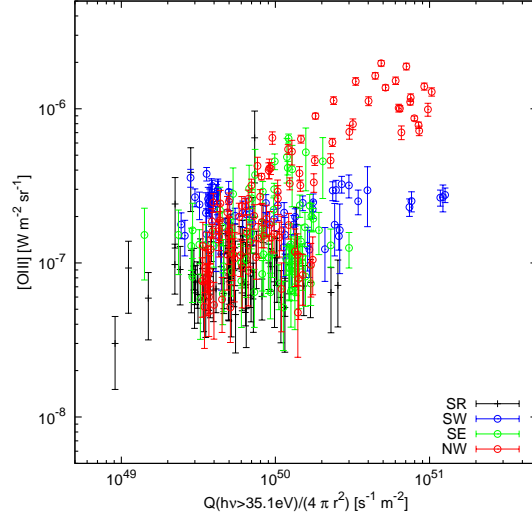


Fig. 8. [OIII] 88μm line intensity plotted as a function of the O⁺-ionizing (> 35.12 eV) photon flux, which is calculated for each observing point by summing the contribution of the cataloged massive stars shown in figure 7 without correcting for any absorptions.

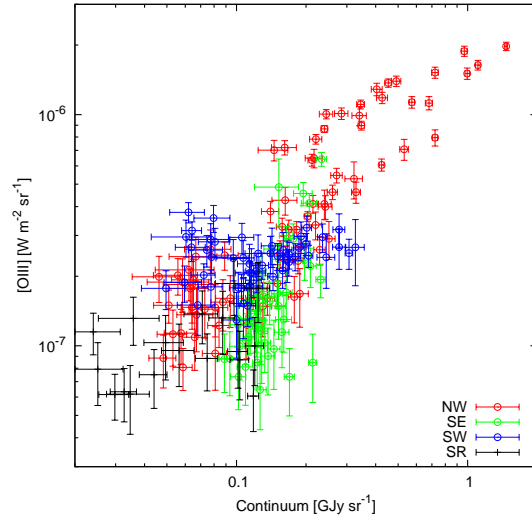


Fig. 9. Scatter plot between the [OIII] line intensity and the far-IR continuum emission at 88 μm, both of which are obtained with FIS-FTS. The colors of data points are the same as in figure 4.

The ionization of the SW region does not seem to be related to the central sources in the 30 Dor region as seen in figure 6. In figure 9, all the data points seem to follow the global trend of correlation. By looking locally in detail, however, the SW group has a much weaker dependence of the [OIII] intensity on the far-IR continuum emission, i.e. no clear correlation between the [OIII] and the dust emission, suggesting that the dust and ionized gases are not mixed well in this region. As described above, most data points of the SW region are located on the supershell of the supernova remnants 30 Dor C (Townesley et al. 2006). Then, a large fraction of dust in the supershell may have been destroyed by the supernovae.

6. Summary

We have performed spectroscopic surveys of the LMC with AKARI/FIS-FTS with a good spatial resolution of about $1'$. We have analyzed spectral data from the 14 observational points distributed widely around the 30 Dor region on a degree scale. We find that the [OIII] $88\mu\text{m}$ emission is widely extended by more than $10'$ (150 pc) from the central super star cluster, R136. Since the [OIII] line traces highly-ionized gas regions heated by very massive stars, the detection of widely extended [OIII] emission suggests that energetic photons are escaping into regions far from massive stars localized at the center of the 30 Dor region. It is unlikely that a lot of embedded massive stars are hidden in the outer region of 30 Dor. Therefore, a plausible interpretation is that the interstellar medium has a patchy or porous structure around the 30 Dor region, so that high-energy photons can pervade into wider areas. This is also supported by a good correlation between the [OIII] emission and the far-IR continuum emission, suggesting that the gas and dust are well mixed in the highly-ionized region where the dust survives in clumpy dense clouds shielded from the energetic photons.

We would express many thanks to an anonymous referee for giving us important comments. We thank all members of the AKARI project. Particularly, we express our gratitude to the AKARI data reduction team for their dedicated work in generating the TSD, and developing data analysis pipelines. AKARI is a JAXA project with the participation of ESA. This work is based in part on observations made with the Spitzer Space Telescope, which is operated by the Jet Propulsion Laboratory, California Institute of Technology under a contract with NASA. This work also made use of data product from the Southern H-Alpha Sky Survey Atlas (SHASSA), which is supported by the National Science Foundation.

References

- Bamba, A., Ueno, M., Nakajima, H., & Koyama, K. 2004, *ApJ*, 602, 257-263
 Bonanos, A. Z. et al. 2009, *AJ*, 138, 1003-1021
 Gaustad, J. E., McCullough, P. R., Rosing, W., & Van Buren, D. 2001, *PASP*, 113, 1326-1348
 Indebetouw, R. et al. 2009, *ApJ*, 694, 84-106

- Kawada, M. et al. 2007, PASJ, 59, S389-S400
- Kawada, M. et al. 2008, PASJ, 60, S389-S397
- Kennicutt, R. C., Jr. 1984, ApJ, 287, 116-130
- Madden, S. C., Galliano, F., Jones, A. P., & Sauvage, M. 2006, A&A, 446, 877-896
- Massey, P., & Hunter, D. A. 1998, ApJ, 493, 180-194
- Meixner, M. et al. 2006, AJ, 132, 2268-2288
- Mendoza, C. 1983, in Planetary nebulae; Proceedings of the Symposium, London, England, August 9-13, 1982, (D. Reidel Publishing Co., Dordrecht) 143-172.
- Murakami, H. et al. 2007, PASJ, 59, S369-S376
- Murakami, N. et al. 2010, PASJ, 62, 1155-1166
- Onaka, T. et al. 2007, PASJ, 59, S401-S410
- Peck, A. B., Goss, W. M., Dickel, H. R., Roelfsema, P. R., Kesteven, M. J., Dickel, J. R., Milne, D. K., & Points, S. D. 1997, ApJ, 486, 329-337
- Poglitsch, A., Krabbe, A., Madden, S. C., Nikola, T., Geis, N., Johansson, L. E. B., Stacey, G. J., & Sternberg, A. 1995, ApJ, 454, 293-306
- Rubin, D. et al. 2009, A&A, 494, 647-661
- Rubio, M., Barbá, R. H., Walborn, N. R., Probst, R. G., García, J., & Roth, M. R. 1998, AJ, 116, 1708-1718
- Selman, F., Melnick, J., Bosch, G., & Terlevich, R. 1999, A&A, 347, 532-549
- Smith, R. C., Leiton, R., & Pizarro, S. 2000, in Stars, gas and dust in galaxies: Exploring the Links, ASP Conference Proceedings, Vol. 221. Ed. Alloin, D., Olsen, K., and Galaz, G., San Francisco, 83-86.
- Townsley, L. K., Broos, P. S., Feigelson, E. D., Brandl, B. R., Chu, Y.-H., Garmire, G. P., & Pavlov, G. G. 2006, AJ, 131, 2140-2163
- Vacca, W. D., Garmany, C. D., & Shull, J. M. 1996, ApJ, 460, 914-931
- Vermeij, R., Damour, F., van der Hulst, J. M., & Baluteau, J.-P. 2002, A&A, 390, 649-665
- Vermeij, R., & van der Hulst, J. M. 2002, A&A, 391, 1081-1095
- Yamaguchi, H., Bamba, A., & Koyama, K. 2009, PASJ, 61, S175-S181